MRS Advances © 2020 Materials Research Society
DOI: 10.1557/adv.2020.89

Effect of cooling profile on crystalline phases, oxidation state, and chemical partitioning of complex glasses

Authors: J. Marcial,[1,2] O. K. Neill,[3] M. Newville,[4] J. V. Crum,[5] J. McCloy,[1,2,5]

[1]*School of Mechanical and Materials Engineering, Washington State University, Pullman, WA, USA*

[2]*Materials Science and Engineering Program, Washington State University, Pullman, WA, USA*

[3]*School of Earth and Environmental Sciences, University of Michigan, Ann Arbor, MI, USA*

[4]*CARS, University of Chicago, Chicago, IL, USA*

[3]*Pacific Northwest National Laboratory, Richland, WA, USA*

Corresponding author: J. Marcial, email: jose.marcial@wsu.edu

Abstract:

Investigations of the crystallization of aluminosilicate phases within Hanford nuclear waste glasses typically involve subjecting samples to the canister centerline cooling (CCC) schedule. This cooling schedule is representative of the slowest cooling thermal profile which these glasses will experience after the glass is poured into the high level waste (HLW) container. However, few investigations have observed how the crystallization behavior changes by varying the heat treatment schedule. In the present study, three Hanford HLW glasses are subjected to CCC and isothermal heat treatments (IHT) to better understand the evolution of phases and the chemical partitioning due to temperature schedule. Samples were characterized using electron probe microanalysis, X-ray diffraction, micro X-ray fluorescence, and micro X-ray absorption spectroscopy. From IHT, eucryptite and apatite phases were observed which were not observed during CCC. Spatially-resolved measurements demonstrated that the oxidation state of the iron was similar among glass and crystal, and we suggest a mechanism to describe the compositional fluctuations near the crystal-glass interface which influence crystallization.

INTRODUCTION:

Over 200,000 m^3 of nuclear waste is currently stored at the Hanford site located in Washington State, USA [1, 2]. This waste will ultimately be vitrified in a joule-heated ceramic-lined melter, where a slurry composed of liquid waste mixed with glass-forming components is discharged into the melter where it undergoes various batch reactions on heating and finally is converted to melt which is discharged into a container where it cools to form glass. The thermal profile which the melt will experience after pouring into stainless steel canisters will depend on the dimensions of the canister, the pour schedule, the initial melt temperature, the melt thermal diffusivity, etc. [3]. Within the center of the canister, the melt is expected to cool slowly from the melter operating temperature (1150°C) to ambient temperature [3]. For the case of some high-level waste (HLW) glasses, this slow cooling profile has been shown to promote crystallization of aluminosilicate phases, of which nepheline (e.g., $NaAlSiO_4$) is the most-commonly observed. Nepheline crystallization causes significantly reduced chemical durability of the final immobilized waste product, as residual glass after aluminosilicate crystallization is typically enriched in alkali borate species, which tend to react readily with water [4-8].

Previous experiments by Marcial et al. compared the conventional benchtop-scale canister-centerline cooling (CCC) and isothermal heat treatments (IHT) and their influences on the composition and morphology of the resulting nepheline crystals [9, 10]. When comparing among various HLW glasses subjected to the CCC schedule, a correlation was found among the fractions of major elements: Na, K, Ca, Fe, Al, and Si in the starting glass melt and in the final composition of the nepheline crystal. Other elements, such as boron, zirconium, and phosphorous, were found to partition out of the nepheline crystals regardless of their original fraction in the melt.

For the case of IHT, one HLW glass composition, denoted as 'A4', was subjected to five different isothermal dwells in the range of 1050-750°C for durations of 3-30 hours [9]. It was found that the so-called "degree of undercooling" affected the morphology of the resulting aluminosilicate crystals but not the measured compositions of the precipitated crystals. Samples subjected to a "lower" degree of undercooling (rapidly cooled from melt to ~75°C below the liquidus) featured faceted, polygonal crystals. Samples subjected to a "higher" degree of undercooling (rapidly cooled from melt to ~150°C below the liquidus) featured dendritic crystals.

Two questions remained following the previous studies of CCC and IHT thermal schedules: (i) can features be observed near the glass-crystal interface that describe the propensity for crystallization as a function of temperature and (ii) how do the phase relationships continue to evolve as a function of heat treatment schedule? This work seeks to provide answers to these questions using X-ray diffraction (XRD) and microstructural imaging. This imaging was performed by scanning electron microscopy energy-dispersive spectroscopy (SEM-EDS) and wavelength-dispersive spectroscopy (SEM-WDS), i.e. electron probe microanalysis (EPMA), as well as synchrotron-based micro X-ray fluorescence (μ-XRF) and micro X-ray absorption near-edge structure (μ-XANES).

Methods

Sample preparation

In this study, a non-radioactive simulant high-level waste glasses designated as "A4", "NP-K-2", and "NP-Fe-3" were selected for investigation after observation of their unique microstructures upon crystallization [9-11]. Table 1 displays the batched glass compositions. Samples were batched from powder precursors and melted at 1200°C in a

Pt-10% Rh crucible for 1 hour followed by air quenching. Samples were remelted at 1050°C prior to IHT and CCC. Both IHT and CCC were performed using 15 g of glass frit in 1×1×1" Pt-10%Rh boxes. The IHT were performed at 1050, 900, 825, 750, 650, and 550 °C for dwell times ranging 3-30 hours (Figure 1). The 825°C-30 h sample only exhibited evidence of nepheline crystallization on the meniscus and at the glass interface with the platinum crucible (i.e., heterogeneous nucleation); however, crystallization was observed in the bulk for the other samples.

Table 1. Simulated HLW glass compositions in wt%

	A4	NP-K-2	NP-Fe-3
Al_2O_3	24.02	12.95	13.31
B_2O_3	11.99	7.53	7.74
CaO	6.08	1.05	1.08
Fe_2O_3	5.91	9.35	12.95
K_2O	0.14	6.00	0.10
Li_2O	6.77	4.23	4.35
MgO	0.12	0.64	0.66
Na_2O	9.59	19.08	19.62
P_2O_5	1.05	0.94	0.94
SiO_2	30.51	36.12	37.14
ZrO_2	0.4	0.27	0.28
Others*	3.42	1.84	1.83

*includes Ag_2O, As_2O_3, BaO, Bi_2O_3, CdO, Cr_2O_3, CuO, F, MnO, NiO, PbO, Sb_2O_3, SeO_2, SO_3, SrO, TiO_2, and ZnO, see [11, 12]

X-ray diffraction – Rietveld Refinement

XRD was performed with a PANalytical X'Pert PRO MPD X-ray Diffractometer outfitted with a Co-Kα X-ray source operated at 45 kV and 40 mA. The scan parameters were: 20-100° 2θ, 0.05° step, and 20 s dwell. For quantification using Rietveld refinement, 5 wt% of CaF_2 was added as an internal standard to 0.5-5 g of powdered IHT or CCC sample. The nephelines identified through XRD were hexagonal Si-rich nephelines (International Center for Diffraction Data (ICDD) powder diffraction file (PDF) 98-010-8334 or 01-075-2934), rhombohedral nepheline bearing K and Ca (ICDD 05-001-0051) or hexagonal, K-bearing (ICDD 98-003-7356). The gamma-eucryptite was identified as [98-006-6137], the beta-eucryptite was [98-002-2010], the spinel phase was nichromite ($NiCr_2O_4$) [98-002-8835], and the apatite phase was [98-008-1442]. Figure 1 provides the XRD patterns for the samples of A4 that exhibited detectable crystallization of silicate phases.

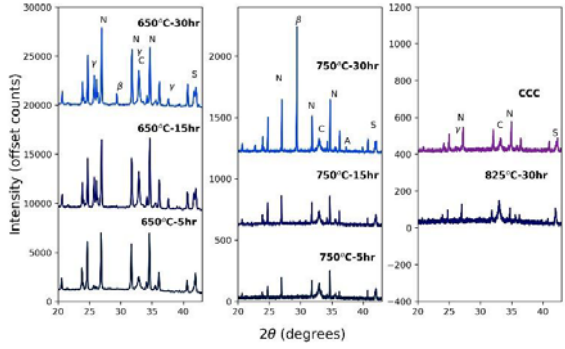

Figure 1. XRD patterns of IHT and CCC heat treated samples of A4. The legends state the heat treatments and the letters represent crystalline phases (N = nepheline, C = CaF_2 internal standard, S = spinel, A = apatite, β = beta-eucryptite, and, and γ = gamma-eucryptite)

Electron probe microanalysis

For EPMA, SEM was coupled with energy-dispersive spectroscopy (SEM-EDS) and/or wavelength-dispersive spectroscopy (SEM-WDS), all samples were sectioned and polished with 400, 800, and 1200 grit SiC paper, followed by 3 then 1 µm diamond pastes. Samples were analyzed on a JEOL JXA-8500F field-emission electron microprobe/scanning electron microscope. Table 2 provides the standard assignments used to calibrate the WDS spectrometers. For WDS maps of the interface of glass to crystals, the beam conditions were 20 kV accelerating voltage, 10 nA probe current and 10 µm spot size. For EDS maps of the interface of glass to crystals, the beam conditions were 15 kV accelerating voltage and 400x magnification. WDS line scans were performed with the spot size of 1.2 µm with the same step size. WDS line scans were rastered from across the interface of glass to crystal and the elements B, Ca, Fe, P, and Zr were analysed for A4; Al, Fe, K, and Na were analysed for NP-K-2; and Al, Ca, and Fe were analysed for NP-Fe-3. Counting was performed on individual spectrometers, to avoid the need to raster over the same area twice (the EPMA system is outfitted for a maximum of 5 simultaneous WDS detector channels). For EDS line scans, measurements were taken with one pass. Figure 2 provides SEM-WDS maps of A4 subjected to canister centreline cooling heat treatment.

Table 2. Spectrometer conditions and standard assignments for SEM-WDS measurements

Element/ X-ray Line	Analyzing Crystal	Line scan Count Time, s	Mapping Count Time, s	Standard
Na Kα	TAP	10	0.5	NIST Glass K-373
Al Kα	TAP	10	0.5	Chromite #5, Australia
Si Kα	PETJ	10	0.5	NIST Glass K-373
Fe Kα	LiF	10	0.5	Pentlandite (Astimex)
Zr Lα	PETH	10	0.5	Zircon #1 (C.M. Taylor)
Ca Kα	PETJ	10	0.5	Apatite, Wilburforce
B Kα	LDE6 (Cr/C Synthetic Multilayer, 2d = 120 Å)	10	0.5	NIST Glass K-490
K Kα	PETH	10	0.5	Orthoclase (MAD-10)
S Kα	PETH	10	0.5	Pentlandite (Astimex)
P Kα	PETJ	10	0.5	Apatite, Wilburforce

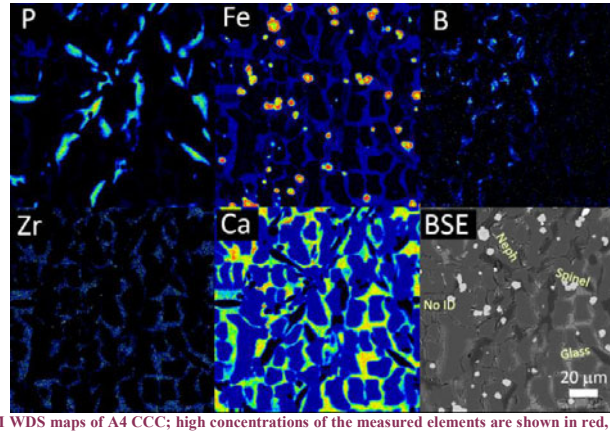

Figure 2. SEM WDS maps of A4 CCC; high concentrations of the measured elements are shown in red, moderate concentrations in yellow, and low concentrations in blue. BSE indicates backscattered electron image

Synchrotron micro X-ray fluorescence and micro X-ray absorption

Spatially-resolved spectroscopic measurements of CCC heat-treated A4 glass was performed using micro X-ray fluorescence (μ-XRF) and micro X-ray absorption near-edge structure (μ-XANES) at the GSECARS (13-ID-E) beamline of the Advanced Photon Source of Argonne National Laboratory. The measurement geometry implemented was fluorescence mode, which allowed for simultaneous acquisition of μ-XRF and μ-XANES. The scan parameters for μ-XANES were: scan range: -50 to +250 eV around the Fe K-edge (E_0 = 7111 eV) with a Si(111) monochromator. The scan parameters for μ-XRF were 1x1 mm areas, interrogated with a spatial resolution of 2 micron/pixel and a dwell time of 20 ms per pixel. X-ray energies were selected to fluoresce the K-lines of Fe, Ca, and Cr. The A4-CCC sample was the same polished thin section used for EPMA.

Discussion

Effect of heat treatment on phase evolution of A4 HLW glass

In this section, the influence of heat treatment schedule on the phase assemblage will be further elucidated for one HLW glass composition. Typically, the CCC schedule is treated as the "worst case" scenario for crystallization; however, in the event that future policies tolerate a fraction of crystallization, it is beneficial to know the effects at various temperatures for various times in order to understand the crystallization behavior at different locations within the stainless-steel canister.

The compositional maps of A4-CCC provided in Figure 2 demonstrate the complex microstructures exhibited by HLW samples, as previously discussed [9, 10]. The presence of phosphorus-, boron-, zirconium-, and iron-enriched phases were observed to form among branches of nepheline dendrites. Based on the XRD results in Figure 1, a time-temperature-transformation (TTT) diagram was constructed and is provided in Figure 3. Though phase information for the unidentified phase in Figure 2 has not fully been determined, based on the final position of the CCC schedule on the TTT diagram and the weak diffraction peak centered near 27° 2Θ in Figure 1, evidence suggests that this phase is gamma-eucryptite. Literature evidence exists for the substitution of phosphorus into eucryptite phases, in particular the $LiAlSiO_4$-$AlPO_4$ solid solution [13, 14]. Due to the low atomic number of Li, it cannot be detected by EDS or WDS; however, other methods may be employed in the future to understand the spatial distribution of Li, including secondary-ion mass spectrometry (TOFSIMS or NanoSIMS) [15]. Regardless of precise crystal chemistry of this phase, previous semi-quantitative EDS analysis suggested that a significant fraction of this phase was silica, suggesting that crystallization of this phase would have a negative impact on the chemical durability of the sample as it removes silica from the glass.

Though the TTT diagram in Figure 3 is based on sparse data and only for one composition, it represents one of the few TTT diagrams obtained for nuclear waste glasses. Another such TTT diagram was presented several decades ago by Jantzen and Brown [16], and more recently by Billings and Edwards [17, 18]. These studies modeled the nepheline-spinel psuedobinary phase diagram for high-level waste borosilicate glasses. Through their investigation of the crystallization kinetics of nuclear waste glasses, Jantzen and Brown observed that hypoeutectic compositions were found to form readily in various silicate phases, some of which were also Li-bearing [16]. Recently, McClane et al. measured nucleation and growth curves for similar HLW glasses and determined that the temperature of the maximum nucleation rate of nepheline was 500-650°C and the temperature of maximum growth rate was 600-750°C [19].

Interestingly, it was observed that nepheline crystallization proceeds during relatively short timescales (~5 hours). Nepheline was not observed to transform to or from its carnegieite polymorphs at any temperature or time tested. On the other hand, eucryptite was observed to transform from the stuffed-cristobalite structure (γ-eucryptite) to the stuffed-β-quartz structure (β-eucryptite) after 30 hours of isothermal heating at 650-750°C. This transformation has been observed for pure crystalline samples at temperatures near 1000°C [20]. In addition to the phase transformation of eucryptite, an apatite phase (containing Ca and P) was found to stabilize after 30 hours at 750°C.

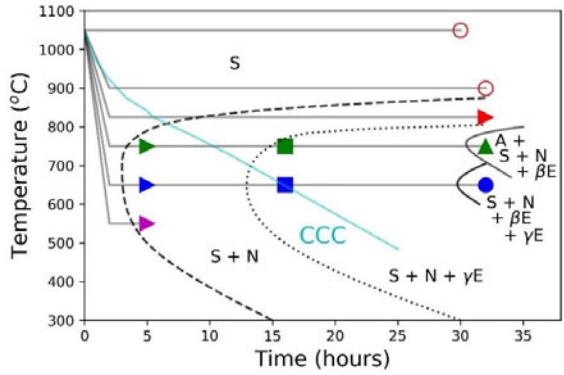

Figure 3. Schematic representation of TTT diagram of A4-composition HLW glass obtained using XRD measurements of samples subjected to IHT and CCC heat treatments. The letters represent crystalline phases (N = nepheline, S = spinel, A = apatite, βE = beta-eucryptite, and γE = gamma-eucryptite)

Improved understanding the influence of the oxidation state of the glass is an important parameter to understand since it is intimately related to structural properties of the glass-forming melt such as the number of non-bridging oxygens which influence the connectivity of the glass network and affect macroscale properties such as the glass density and melt viscosity [21]. Viscosity of the melt, in turn, influences the mobility of ions in the melt thereby also affecting the crystallization behavior [22]. The oxidation state of the material after heat-treating is challenging to understand due to it being a multiphase mixture. In the case of HLW samples, the major redox-sensitive species is iron. On one hand, high-level waste glasses are typically assumed to exhibit minor reduction of iron as a function of increased temperature, which is accompanied by the release of oxygen from the melt [23]. However, on the other hand, the crystallization of spinels could buffer the melt by accepting the small amount of Fe^{2+} in addition to Fe^{3+} into the crystalline lattice. Although it is not readily evident in the μ-XRF map in Figure 4, HLW glasses contain approximately 5-12 wt% Fe_2O_3 and the nepheline which crystallizes in A4 glass after CCC is 1.32 wt% Fe_2O_3 [10]. Iron is known to enter the nepheline lattice in Al sites as high as 19 wt% Fe_2O_3 for $NaAl_xFe_{1-x}SiO_4$ glass-ceramic systems [24]. By employing μ-XANES, there was no need to deconvolute the individual contributions of the various phases, as would be required for Mössbauer or bulk colorimetric methods. As seen in Figure 4, the residual glass tends to be slightly reduced compared to the nepheline. The different phases are distinguished with the use of an exaggerated color scale in the μ-XRF in Figure 4 as well the exaggerated EPMA map in Figure 2. Most surprisingly, the spinel appears to only feature ferric iron. From previous analyses, it was observed that the spinel in these HLW samples also features di-valent elements such as Mg^{2+} and Ni^{2+} [9]. The iron-bearing precursor used for this glass was hematite ($Fe^{3+}{}_2O_3$) and the sample was melted in air which would largely influence the

oxidation state of the iron in the melt. In HLW feed, the oxidation state of the iron during melting may be influenced by various parameters. First, the feed contains significant amounts of nitrate salts, which are known to oxidize iron. Second, the feed may feature hypophosphite, sucrose, or oxalate additives, which can reduce iron. Finally, the iron is present in the waste as a partially-hydrated iron hydroxide which may itself have some mixed valency [25].

Mapping by µ-XRF was used to verify that the regions interrogated by µ-XANES belonged to the correct phases, see Figure 4. Though µ-XRF can be used to obtain high-resolution compositional mapping, in Figure 4 it demonstrates that the glass and nepheline both contain Ca, consistent with Ca being observed previously in the hexagonal site of nepheline (which yields a vacancy in the lattice for charge compensation) [26], and the spinels feature varying concentrations of Fe and Cr. The next section will further discuss compositional relationships among the glass and nepheline as observed through EPMA.

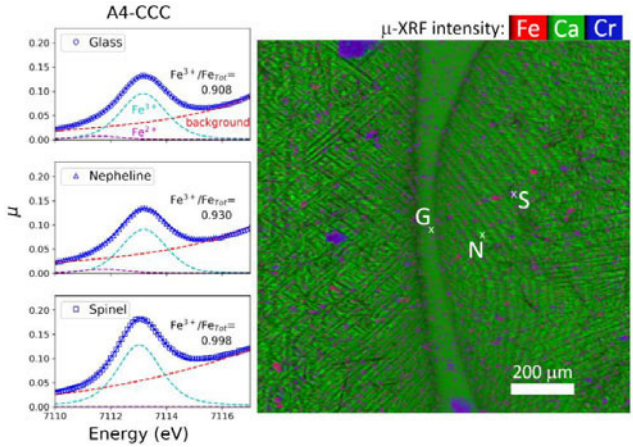

Figure 4. (Left) Fitting results for Pre-edge feature of Fe K-edge µ-XANES demonstrating the difference in iron oxidation state in various phases present in A4-CCC sample and (right) µ-XRF intensity map for Fe, Ca, and Cr where the relative amount of each component is given by the intensity of red (Fe), green (Ca), or blue (Cr). The locations marked were used for µ-XANES. In the µ-XRF map, G = glass, N = nepheline, and S = spinel

Investigation of microscale chemical partitioning through electron microprobe

Figures 5 & 6 provide high-resolution WDS maps of the samples NP-K-2 and NP-Fe-3 (see Section 2.1.3 for compositions) which underwent CCC. Figure 7 provides SEM BSE images of isothermally heat treated A4 in the regions where line scans were performed and Figure 8 provides the WDS compositional line scans and Figure 9 provides the EDS compositional line scans.

In Figures 5 & 6 it is apparent that compositional gradients exist along the interface of the glass and the nepheline crystals (especially in the Fe and Al) as seen in Figure 5 for K, Fe, and Na. Though the compositional gradients within the nepheline crystals are not well resolved in Figure 2, compositional variations within the nepheline crystals and glass near the interface are present in the IHT samples of A4 (see the WDS line scans presented in Figure 8 and EDS line scans in Figure 9). In Figure 8, a sharp deflection in the measured compositions of Si, Al, Fe, and Ca species, presented as oxide weight percent, is observed at the glass-crystal interface. A significant difference among

the glass-forming melt and the nepheline were previously predicted to exist [9, 10] but these line scans allow us to observe that a sharp interface exists on the order of 3-5 µm.

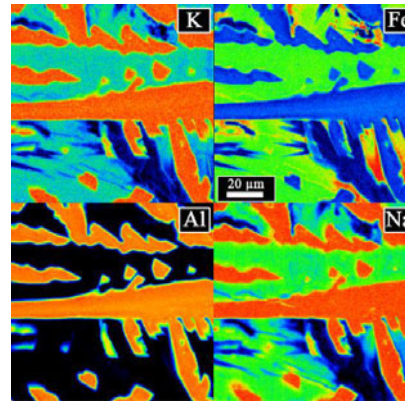

Figure 5. SEM WDS maps of NP-K-2 CCC; BSE indicates backscattered electron image.

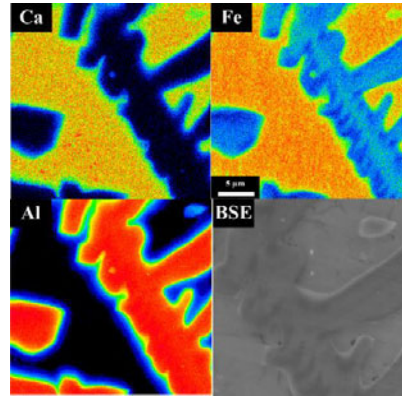

Figure 6. SEM WDS maps of NP-Fe-3 CCC; BSE indicates backscattered electron image.

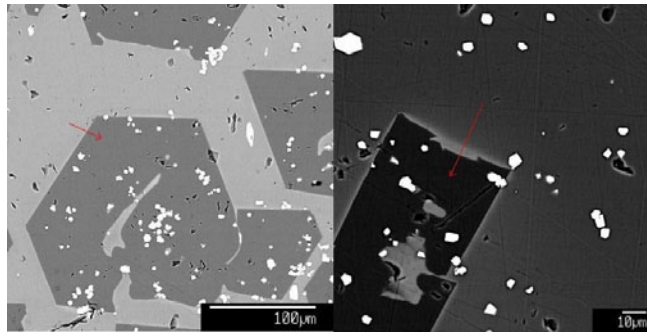

Figure 7. SEM-BSE images for (left) A4-750°C 30 hr and (right) A4-825°C 30 hr. The red arrows on the images indicate the path over which the beam was rastered during the acquisition of the line scans. Note the skeletal nature of the nepheline crystals indicating high undercooling. Bright crystals within the nephelines are spinels.

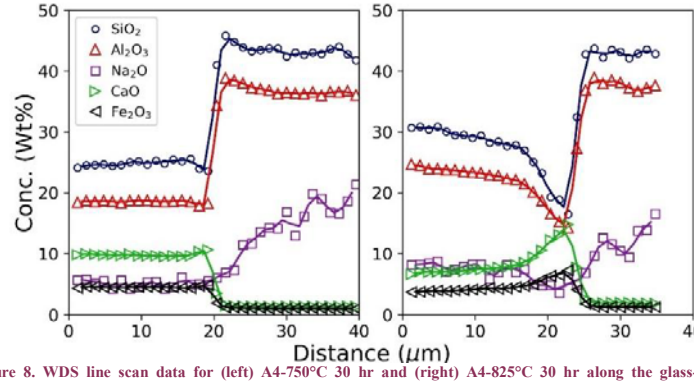

Figure 8. WDS line scan data for (left) A4-750°C 30 hr and (right) A4-825°C 30 hr along the glass-crystal interface shown in Figure 7.

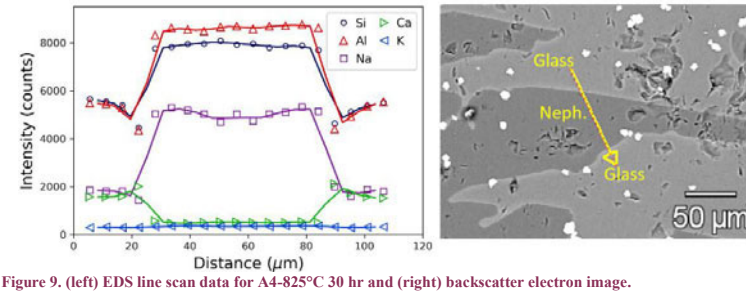

Figure 9. (left) EDS line scan data for A4-825°C 30 hr and (right) backscatter electron image.

The abrupt spatial change in concentrations of Al, Si, Ca, and Fe seen in Figure 8 was due to the equilibrium compositional change during crystallization, as would be observed in the equilibrium phase diagram as the temperature dropped below the liquidus. The difference among the compositions of the melt and crystal could be described using a transect line in the equilibrium phase diagram and following the intersection point with the nepheline phase and melt phase down to the composition axis as described with the so-called "lever rule", see Figure 10.

In addition to the abrupt compositional variation which accompanies equilibrium crystallization, the WDS line scans in Figure 8 exhibit a peak in the Ca and Fe signal and a negative peak in the Si and Al signal near the crystal-glass interface which is attributed to the presence of a boundary layer which encircles the nepheline crystals. These peaks appear larger for the 825°C than for the 750°C. Based on the XRD data in Figure 1, it would appear that the size of the boundary layer is correlated to the extent of crystallization. The larger the boundary layer (given by the peak size in the WDS line scan) corresponds to the low degree of crystallization (given by the peak height of the nepheline phase). It is predicted that this boundary or 'buffer' region acts to reduce the extent of crystallization by increasing the path length required for diffusion from the bulk melt into the crystal as depicted schematically in Figure 10.

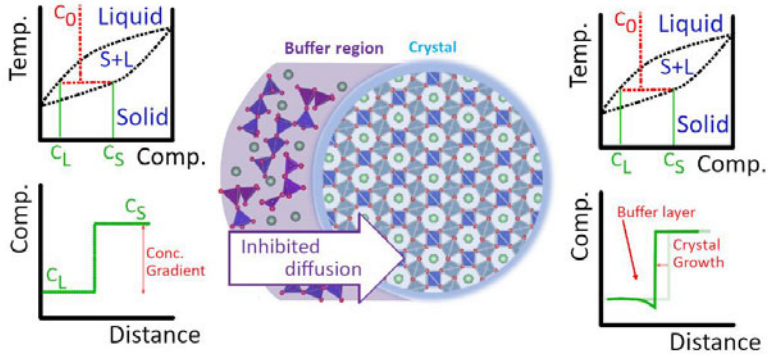

Figure 10. Schematic depiction of the compositional partitioning at the interface of crystal and "residual glass".

The product performance relevance of non-uniform composition for the large-scale vitrification of nuclear waste would require further experimentation, but is similar to the effects already considered when discussing the chemical durability of "residual" glass. On one hand, the chemically partitioned zone yields a glass that is depleted in Al and Si relative to the bulk glass; however, this glass layer is only a few micrometers thick and would likely be more concerning for systems whose crystals feature a high surface-to-volume ratio such as the dendritic crystals observed for A4, NP-K-2, and NP-Fe-3 after CCC heat treatment. The chemically-partitioned layer observed in the crystal at the interface is academically interesting, but the crystal phases typically exhibit much higher chemical durabilities than the bulk glass. This method of investigating the evolution of crystalline phases as a function of heat treatment schedule may be of interest to other countries seeking to immobilize their waste streams in glass-ceramic waste forms, especially those seeking to immobilize rare-earth elements in apatite-like phases.

The influence of spinel crystals on the nucleation of nepheline and other aluminosilicates can depend on the glass. Previous authors have performed transmission electron microscopy selected area diffraction (TEM-SAD) on quenched HLW melts, i.e. the baseline composition of the NP glasses of Figures 8 & 9, and found electron diffraction patterns characteristic of nepheline with no spinels present, suggesting that nepheline crystallized without the presence of spinel in the NP glasses [27]. This previous finding is consistent with EPMA maps of NP-K-2 and NP-Fe-3 shown in Figures 8 & 9, where few spinel crystals were found near the nepheline dendrite branches. For the A4 sample, however, spinels were found to exist in the bulk glass, between nepheline branches, and apparently within the nepheline crystals (see Figures 2 & 7). As seen in Figure 3, spinel crystals exist above the nepheline liquidus, at temperatures as high as 1050°C.

Conclusion

The influence of heat treatment schedule on the microstructural characteristics of composition and phase were investigated for high-level nuclear waste glasses. Spinel and nepheline were the most abundant phases to crystallize. However, new evidence was provided that describes the distribution of other phases including eucryptite and apatite as a function of temperature and time. Lastly, a mechanism was proposed to describe the distribution of chemical species at the glass-crystal interface that influences the extent of crystallization as a function of dwell temperature.

Acknowledgements

This research was supported by the Department of Energy's Waste Treatment and Immobilization Plant Federal Project Office, contract number DE-EM002904, under the direction of Dr. Albert A. Kruger. Electron microprobe analyses were performed at the Peter Hooper GeoAnalytical Laboratory of the WSU School of the Environment. Thanks to Mahmood Abusamha for assistance preparing samples. This research used resources of the Advanced Photon Source, a U.S. Department of Energy (DOE) Office of Science User Facility operated for the DOE Office of Science by Argonne National Laboratory under Contract No. DE-AC02-06CH11357.

References:

1. A. A. Kruger, Proc. for Waste Manag. Conf. (1), 1-15 (2013).
2. A. Goel, J. McCloy, R. Pokorny and A. A. Kruger, J. Non-Cryst. Solids X **4**, 1-19 (2019).
3. J. Amoroso, SRNL-STI-2011-00546 (2011).
4. B. J. Riley, P. Hrma, J. Rosario and J. D. Vienna, Ceram. Trans. **132**, 257-265 (2001).
5. J. S. McCloy, C. Rodriguez, C. Windisch, C. Leslie, M. J. Schweiger, B. R. Riley and J. D. Vienna, in *Advances in Materials Science for Environmental and Nuclear Technology* (John Wiley & Sons, Inc., 2010), pp. 63-76.
6. C. M. Jantzen and D. E. Bickford, in *Materials Research Society Proceedings* (Pittsburgh, PA, USA, 1985), Vol. 44, pp. 11.
7. T. M. Besmann, K. E. Spear and E. C. Beahm, MRS Proc. **608** (2011).
8. C. P. Rodriguez, J. McCloy, M. J. Schweiger, J. V. Crum and A. Winschell, Report No. PNNL-20184, 2011.
9. J. Marcial, J. McCloy and O. Neill, in *Symposium on Scientific Basis for Nuclear Waste Management XX* (Mater. Res. Soc. Symp. Proc., Boston, MA, USA, 2015).
10. J. Marcial, J. Crum, O. Neill and J. McCloy, Amer. Mineral. **101** (2), 266-276 (2016).
11. P. Hrma, M. J. Schweiger, C. J. Humrickhouse, J. A. Moody, R. M. Tate, T. T. Rainsdon, N. E. TeGrotenhuis, B. M. Arrigoni, J. Marcial, C. P. Rodriguez and B. H. Tincher, Ceramics-Silikaty **54**, 193-211 (2010).
12. H. Li, J. D. Vienna, P. Hrma, D. E. Smith and M. J. Schweiger, in *Scientific Basis for Nuclear Waste Management XX* (Mater. Res. Soc. Symp. Proc., Pittsburgh, PA, 1997), Vol. 465, pp. 261-268.
13. R. M. Tindwa, A. J. Perrotta, P. Jerus and A. Clearfield, Mat. Res. Bull. **17** (7), 873-881 (1982).
14. V. Dondur, R. Dimitrijevic and N. Petranovic, J. Mater. Sci. **23** (11), 4081-4084 (1988).
15. Z. Wang, J. Liu, Y. Zhou, J. Neeway, D. K. Schreiber, J. V. Crum, J. V. Ryan, X. L. Wang, F. Wang and Z. Zhu, Surf. Interface Anal. **48**, 1392-1401 (2016).
16. C. M. Jantzen and K. G. Brown, J. Amer. Ceram. Soc. **90** (6), 1880-1891 (2007).
17. A. Billings and T. T. Edwards, SRNL-STI-2009-00025 (2009).
18. A. Billings and T. T. Edwards, SRNL-STI-2010-00373 (2010).
19. D. L. McClane, J. W. Amoroso, K. M. Fox and A. A. Kruger, J. Non-Cryst. Solids **505**, 215-224 (2019).
20. P. Norby, Zeolites **10** (3), 193-199 (1990).
21. D. B. Dingwell and D. Virgo, Geochim. Cosmochim. Acta **51** (1), 195-205 (1987).
22. P. Hrma, J. Non-Cryst. Solids **356**, 3019-3025 (2010).
23. M. Hujova, R. Pokorny, J. Klouzek, S. M. Lee, J. J. Traverso, M. J. Schweiger, A. A. Kruger and P. Hrma, Int. J. Appl. Glass Sci. **9**, 487-498 (2018).
24. M. Ahmadzadeh, J. Marcial and J. McCloy, J. Geophys. Res. Solid Earth **122** (4), 2504-2524 (2017).
25. K. S. Matlack, C. Viragh, W. Kot and I. L. Pegg, VSL-13R33430-1 (2015).
26. A. Deshkar, J. Marcial, S. A. Southern, L. Kobera, D. L. Bryce, J. S. McCloy and A. Goel, J. Am. Ceram. Soc. **100** (7), 2859-2878 (2017).
27. H. Li, P. R. Hrma, J. D. Vienna, M. Qian, Y. Su and D. E. Smith, J. Non-Cryst. Solids **331** (1-3), 202-216 (2003).